

Manganese-Cobalt Hexacyanoferrate Cathodes for Sodium-ion Batteries

Mauro Pasta^{1,2†}, Richard Y. Wang^{1†}, Riccardo Ruffo³, Ruimin Qiao⁴, Hyun-Wook Lee¹, Badri Shyam⁵, Minghua Guo^{4,6}, Yayu Wang⁶, L. Andrew Wray⁷, Wanli Yang⁴, Michael F. Toney⁵ and Yi Cui^{1,8*}

¹Department of Materials Science and Engineering, Stanford University, Stanford, California 94305, USA.

²Department of Materials, University of Oxford, Oxford, OX1 3PH, UK.

³Dipartimento di Scienza dei Materiali, Università degli Studi di Milano-Bicocca, Via Cozzi 53, 20125 Milano, Italy.

⁴Advanced Light Source, Lawrence Berkeley National Laboratory, Berkeley, CA 94720, USA

⁵Stanford Synchrotron Radiation Lightsource, SLAC National Accelerator Laboratory, Menlo Park, California 94025, USA.

⁶State Key Lab of Low-Dimensional Quantum Physics, Department of Physics, Tsinghua University, Beijing 100084, P.R. China.

⁷Department of Physics, New York University, New York, New York 10003, USA

⁸Stanford Institute for Materials and Energy Sciences, SLAC National Accelerator Laboratory, 2575 Sand Hill Road, Menlo Park, California 94025, USA.

Prussian Blue analogues (PBAs) have shown promise as electrode materials for grid-scale batteries because of their high cycle life and rapid kinetics in aqueous-based electrolytes. However, these materials suffer from relatively low specific capacity, which may limit their practical applications. Here, we investigate strategies to improve the specific capacity of these materials while maintaining their cycling stability and elucidate mechanisms that enhance their electrochemical properties. In particular, we have studied the electrochemical and structural properties of manganese hexacyanoferrate (MnHCF_e) and cobalt hexacyanoferrate (CoHCF_e) in an aqueous, sodium-ion electrolyte. We also studied manganese-cobalt hexacyanoferrates (Mn-CoHCF_e) solid solutions with different Mn/Co ratios that combine properties of both MnHCF_e and CoHCF_e. The materials have the characteristic open-framework crystal structure of PBAs, and their specific capacities can be significantly improved by electrochemically cycling (oxidizing and reducing) both the carbon-coordinated Fe and the nitrogen-coordinated Co or Mn

* Corresponding Author: yicui@stanford.edu

† These authors contributed equally

ions. In situ synchrotron X-ray diffraction studies and ex situ soft X-ray absorption spectroscopy combined with an in-depth electrochemical characterization provide insight into the different electrochemical properties associated with the Fe, Co, and Mn redox couples. We show that cycling the C-coordinated Fe preserves the crystal structure and enables the outstanding kinetics and cycle life previously displayed by PBAs in aqueous electrolytes. On the other hand, the N-coordinated Co and Mn ions exhibit a slower kinetic regime due to structural distortions resulting from the weak N-coordinated crystal field, but they still contribute significantly towards increasing the specific capacity of the materials. These results provide the understanding needed to drive future development of PBAs for grid-scale applications that require extremely high cycle life and kinetics.

Introduction

Renewable energy sources such as solar and wind power are fundamentally different from conventional fossil-fuel energy generation because of their inherent intermittency¹. The power output of solar and wind farms is limited both by diurnal cycles and short-term seconds-to-minutes volatility due to rapid changes in cloud cover and wind conditions². Energy storage is needed both for diurnal load balancing and the smoothing of intermittent spikes or drops in power production². Energy storage systems used for this application must be deployable across the grid, have extraordinarily long cycle life, be capable of high power charge and discharge in minutes, have very high energy efficiency, and above all, have low capital and lifetime costs^{3,4}. A new kind of energy storage technology is needed for short-term grid storage applications, as existing technologies struggle to meet the needs of these applications at a reasonable price^{1,2,5,6}.

Recently, promising results have been obtained with a new family of battery electrode materials based on the common, inexpensive Prussian Blue pigment and are commonly known as Prussian Blue analogues (PBAs)⁷⁻¹³. Their open framework crystal structure is composed of a face-centered cubic framework of transition metal cations octahedrally coordinated to hexacyanometallate groups (**Figure 1a**)¹⁴⁻¹⁶. Large interstitial "A sites" within the structure can accommodate zeolitic water or alkali insertion ions. This results in a general chemical formula of $A_xP[R(CN)_6]_{1-y}\square_y \cdot nH_2O$, where A is an alkali cation, P is the N-coordinated transition metal cation, $[R(CN)_6]$ is the hexacyanometallate anion, and \square represents a hexacyanometallate vacancy. Both the N-coordinated and C-coordinated transition metals can be electrochemically active in this structure. In this work, we adopt the following notation: $P^{I/J}-N\equiv C-R^{K/L}$, where I, J, K, and L are valence states of the P and R cations.

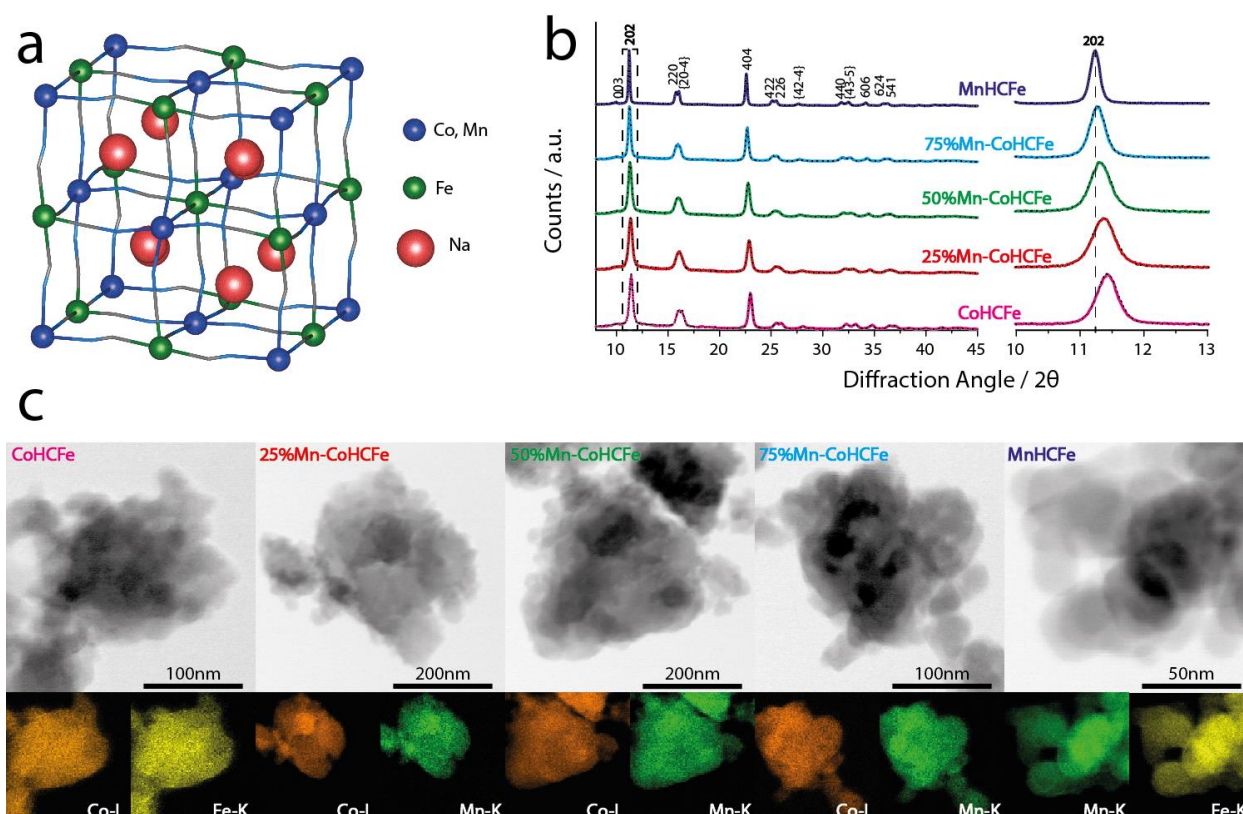


Figure 1. Physicochemical Characterization of the Mn-CoHCFE solid solutions. The as-synthesized powders have a (a) rhombohedral lattice with the R-3m space group. The light blue lines correspond to the N atoms, and the gray lines correspond to the C atoms (omitted for clarity). The space group is confirmed by (b) Le Bail fitting of the synchrotron X-ray powder diffractograms. Transmission electron microscopy (TEM) images (c) show that the Co-containing particles are made of smaller crystallites that are not seen in MnHCFE. Energy-dispersive X-ray spectroscopy (EDS) mapping further confirms the uniform distribution of Co (orange), Mn (green), and Fe (yellow) in each particle characteristic of a solid solution.

The PBA framework structure has wide channels between the A sites ($\langle 100 \rangle$ directions), allowing for the rapid insertion and removal of monovalent alkali cations and multivalent cations¹⁷ from aqueous solutions. In addition, there is little lattice strain during cycling because the A sites are larger than the ions that are inserted and removed from them⁹. Extremely stable copper and nickel hexacyanoferrate cathodes^{9,10} paired with a double-layer capacitor¹⁸ or a manganese hexacyanomanganate¹⁹ PBA anode form full batteries with outstanding cycle life, energy efficiency, and power output.

A limitation of the previously reported hexacyanoferrate cathodes is a low specific capacity of about 60 mAh g⁻¹ that constrains the specific energy and power of the full battery. However, their theoretical specific capacity is more than double (171 mAh g⁻¹ for Prussian Blue²⁰). Access to the full capacity is limited by two factors. First, in these materials, only the C-coordinated Fe is electrochemically active. This implies that only four out of the eight available A-site nanocavities (**Figure 1a**) contribute to the total capacity. Second, powders synthesized with a conventional co-precipitation method contain about 30% of hexacyanoferrate vacancies²¹. Each missing [Fe(CN)₆] lowers the potential capacity that can be utilized.

Moreover, water molecules bond to the N-coordinated transition metal ions around a hexacyanoferrate vacancy²², which further decreases the specific capacity.

In this study, we optimized a synthesis procedure to reduce the vacancies within PBAs while preserving the essential high-symmetry open framework structure. We investigated the electrochemical and structural properties of manganese hexacyanoferrate (MnHCF_e), cobalt hexacyanoferrate (CoHCF_e), and mixtures of the two. In both of these materials, the N-coordinated transition metal ions (Mn and Co, respectively) are electrochemically active in the electrochemical stability window of the aqueous electrolyte. We studied how each of the redox couples contributes to the specific capacity, the relative performance and stability of each couple, and mechanisms that may either limit or enhance the performance associated with each. These experiments provide a broader understanding of methods to increase specific capacities in PBAs and explain how such methods may either degrade or preserve the properties that make PBAs suitable for grid-scale batteries.

Results

Physicochemical characterization of the as-synthesized Co-MnHCF_e powders.

MnHCF_e, CoHCF_e, and the 25% Mn, 50% Mn, 75% Mn-CoHCF_e solid solutions were synthesized in their reduced form (Mn^{II}, Co^{II}—N≡C—Fe^{II}) and with a low vacancy content by adapting a method previously proposed by Moritomo et al. for electrodeposited thin films²³. The detailed experimental procedure is reported in the methods section of the **Supporting Information**. The chemical composition of the as-synthesized powders (**Table 1**) was determined by inductively coupled plasma mass spectrometry (ICP-MS), while the water content was analyzed by thermogravimetric analysis (TGA) (**Figure S1**). The composition was also confirmed by TEM-EDX (**Figure S2**). All the materials have a [FeCN]₆ vacancy content ranging from 21 to 8%, which is lower than that of PBAs synthesized with a standard co-precipitation method (30-40%)¹⁹. Pure CoHCF_e and MnHCF_e show a higher vacancy content compared to the solid solutions. This might be due to the different crystallization kinetics associated with their different solubility products. The Mn/Co ratio of the precursors employed in the synthesis is retained in the final product.

Table 1. Physical characterization of the as-synthesized Co-MnHCF_e powders. The powders are produced in their reduced, discharged state (Co^{II}, Mn^{II}—N≡C—Fe^{II}). Le Bail fitting of the synchrotron X-ray diffractograms reported in Figure 1b show that the as-synthesized powders have a rhombohedral lattice (hexagonal setting shown below) with space group R-3m (a=b≠c, α=β= 90°, γ=120°).

Material	Chemical Composition (ICP-MS)	a=b (Å)	c (Å)	a/√2 (Å)	c/√3 (Å)	Crystallite size (nm)
CoHCF_e	Na _{1.54} Co[Fe(CN) ₆] _{0.86} · □ _{0.14} · 2.16H ₂ O	14.852(1)	17.504(2)	10.502	10.106	41
25%Mn-CoHCF_e	Na _{1.76} Mn _{0.26} Co _{0.74} [Fe(CN) ₆] _{0.92} · □ _{0.08} · 2.32H ₂ O	14.915(2)	17.627(4)	10.546	10.177	41
50%Mn-CoHCF_e	Na _{1.70} Mn _{0.50} Co _{0.50} [Fe(CN) ₆] _{0.92} · □ _{0.08} · 2.15H ₂ O	14.974(2)	17.713(3)	10.588	10.227	40
75%Mn-CoHCF_e	Na _{1.53} Mn _{0.75} Co _{0.25} [Fe(CN) ₆] _{0.90} · □ _{0.10} · 2.09H ₂ O	15.021(1)	17.815(3)	10.621	10.285	47
MnHCF_e	Na _{1.33} Mn[Fe(CN) ₆] _{0.79} · □ _{0.21} · 1.88H ₂ O	15.052(1)	17.933(2)	10.643	10.354	81

Synchrotron X-ray powder diffractograms are reported in **Figure 1b**. Le Bail fitting (smooth lines in **Figure 1b**) shows that all the powders have a rhombohedral lattice (hexagonal setting shown) with the R-3m space group. Details of the fit results and full diffractograms are reported in **Table 1** and the **Supporting Information (Figure S3)**. The rhombohedral structure is the result of a distortion of the characteristic, face-centered cubic crystal structure of PBAs along the body diagonal triggered by the asymmetric electrostatic potential induced within the cubic framework²⁴. In fact, each octant (**Figure 1a**) of the unit cell consists of four $[\text{Fe}(\text{CN})_6]^{4-}$ and four Mn^{2+} or Co^{2+} , and therefore the local potential minimum for smaller insertion ions is not at the center of the octant but at a tetrahedral site closer towards the four negatively-charged $[\text{Fe}(\text{CN})_6]^{4-}$. This results in a displacement of the guest sodium ions along the $\langle 111 \rangle$ body diagonal directions that distorts the crystal structure. Previous studies have shown that the displacement of sodium ions can be triggered either by high insertion-ion concentration or by reduced temperature^{23,25}. All the powders have a single rhombohedral phase regardless of the Mn:Co ratio, thus proving that the solid solutions are solid solutions of Mn and Co hexacyanoferrates and not a mixture of two distinct MnHCF and CoHCF phases. This can also be seen in the continuous shift of the XRD peaks (**Figure 1b**). The same was previously observed for the Ni-CuHCF system⁸.

In the inset of **Figure 1b**, the position of the largest diffraction peak (which corresponds to the $\{202\}$ reflections in the hexagonal setting and to the $\{200\}$ reflections in the cubic structure) decreases in 2θ as the Mn content increases. This corresponds to increasing lattice parameter with increasing Mn content. This phenomenon is due to the larger radius of the high-spin, octahedrally coordinated Mn^{2+} (97 pm) compared to the high-spin, octahedrally coordinated Co^{2+} (88.5 pm)²⁶. The average size of the crystallites (details of the analysis are presented in the methods section of the **Supporting Information**), also reported in **Table 1**, is about 40 nm for all the Co-containing materials while the pure MnHCF powder shows crystallites doubled in size. This result is confirmed by the transmission electron microscopy (TEM) images reported in **Figure 1c**, which show that the Co-containing particles are made of smaller crystallites that are not seen in MnHCF. Energy-dispersive X-ray spectroscopy (EDS) mapping (**Figure 1c**) further confirms the uniform distribution of Co, Mn, and Fe in each particle, which is characteristic of a solid solution.

Soft X-ray absorption spectroscopy (sXAS) of Co-MnHCF powders. sXAS probes the unoccupied electronic states in the vicinity of the Fermi energy E_F , which are closely related with crystal fields, chemical bonds, valences, orbital, and spin characters of the material^{27,28}. In particular, the transition metal (TM) *L*-edge sXAS explores the localized $3d$ states through dipole-allowed $2p$ - $3d$ transitions. The sensitivity of the sXAS line shape to the TM oxidation states in a particular ligand field allows a quantitative analysis of the valences of TM atoms²⁹⁻³¹. In PBAs, we have also demonstrated that sXAS provides an especially site-sensitive probe of the TM redox centers, as the N-coordinated and C-coordinated TM ions typically take on different spin states³². The C-coordinated ion experiences a large crystal field splitting due to the ligand, which favors a low-spin (LS) state. Conversely, the N-coordinated ion experiences a much lower crystal field splitting, which encourages a high-spin (HS) state³³.

Fe *L*-edge sXAS of FeC_6 and FeN_6 octahedra can be accurately modeled by atomic multiplet calculations augmented to include both forward and back bonding³⁴. Detailed modeling

parameters are described in the **Supporting Information**. Such an approach allows a direct assignment of the spectroscopic features to the specific site and spin state of Fe atoms³². The two-peak structure of L_3 XAS from C-coordinated Fe^{II} sites in **Figure 2** is indicative of strong backbonding³⁴. For C-coordinated Fe^{III} , an isolated spike of XAS intensity seen at 706 eV represents the excitation of a 2p core electron into a single t_{2g} vacancy and is characteristic of a strong ligand environment that induces a low-spin d^5 configuration^{32,34}.

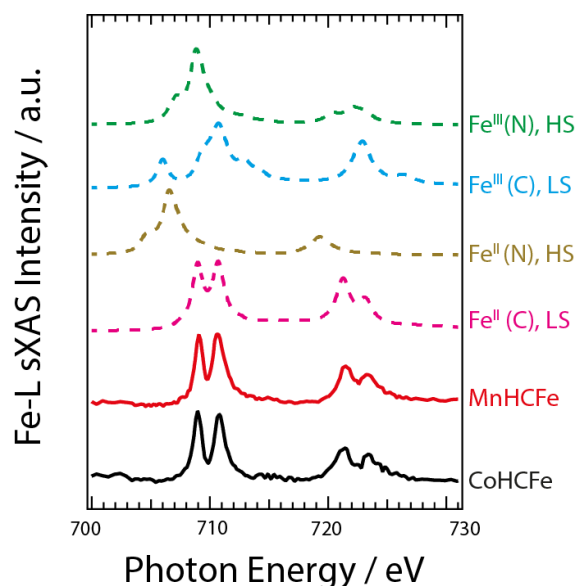


Figure 2. Fe L -edge sXAS spectra of CoHCFE and MnHCFE. Experimental Fe L -edge sXAS spectra (solid lines) of as-synthesized CoHCFE and MnHCFE are compared with calculated spectra (dashed lines) of Fe^{II} and Fe^{III} coordinated octahedrally with C or N from cyano groups. It is demonstrated that Fe is at the reduced state, i.e., Fe^{2+} , and occupies the C-coordinated low-spin site in both CoHCFE and MnHCFE.

Figure 2 compares the Fe L -edge sXAS of the as-synthesized CoHCFE and MnHCFE samples with the theoretical calculations. Overall, the Fe L -edge sXAS spectra consist of two well-separated L_3 (697-709 eV) and L_2 (713-722 eV) absorption features resulting from core-hole spin-orbit coupling. The N-coordinated and C-coordinated Fe^{II} and Fe^{III} display dramatically different sXAS line shapes. By comparing the experimental and simulated spectra in **Figure 2**, it is clearly evident that in both CoHCFE and MnHCFE, Fe is at the reduced state, i.e., Fe^{II} , and occupies the LS, C-coordinated site.

CoHCFE and MnHCFE electrochemistry with sXAS. The cyclic voltammograms (CV) of CoHCFE and MnHCFE in a pH=2, saturated (10M) NaClO_4 aqueous electrolyte are reported in **Figure 3a** and **Figure 3d**, respectively. PBAs are known to be more stable at acidic pH than in neutral and basic conditions, as ligand exchange between the CN^- ligands and OH^- ions results in the dissolution of the Prussian Blue structure³⁵. Perchlorates were selected for their excellent electrochemical stability, especially at very oxidative potentials, combined with a high solubility in water. High electrolyte concentrations, besides minimizing the trace solubility of PBAs, extend the anodic electrochemical stability window of water beyond the thermodynamic 1.08 V versus SHE due to the combination of perchlorate anion adsorption, a decrease in the chemical activity of water, and increased viscosity of the solution³⁶. The experiments were carried out with the experimental setup reported in the in the methods

section of the **Supporting Information**). All the potentials in this manuscript are reported versus the standard hydrogen electrode (SHE).

CoHCFE and MnHCFE powders are synthesized in their reduced states ($\text{Co}^{\text{II}}-\text{N}\equiv\text{C}-\text{Fe}^{\text{II}}$ and $\text{Mn}^{\text{II}}-\text{N}\equiv\text{C}-\text{Fe}^{\text{II}}$) and have open circuit potentials (OCP) of 0.45 and 0.6 V, respectively. Three electrochemical processes are clearly visible at 0.7, 0.75, and 1.2 V in the case of CoHCFE and at 0.8, 0.9, and 1.4 V for MnHCFE. In order to assign redox reactions to each electrochemical process, we performed comprehensive transition metal *L*-edge sXAS studies on a series of CoHCFE and MnHCFE electrodes at different charge states.

CoHCFE and MnHCFE electrodes for the sXAS studies were galvanostatically charged to three different potentials/charge states represented by the blue, red, and green dots in **Figure 3a** and **3d**. Ex situ sXAS at different charge states in **Figure 3b-c** and **3e-f** was used to attribute each electrochemical process to the corresponding transition metal redox couple. The Fe, Co, and Mn *L*-edge sXAS spectra consist of well-separated absorption features resulting from core-hole spin-orbit coupling. The Fe-*L*, Co-*L*, and Mn-*L* absorption profiles of the pristine electrodes resemble the calculated spectra of C-coordinated LS Fe^{II} , N-coordinated HS Co^{II} , and N-coordinated HS Mn^{II} , respectively. Calculated spectra of LS Fe^{III} , LS Co^{III} , and HS Mn^{III} are also plotted for comparison.

On the other hand, the C-coordinated Fe changes its valence state at 1.2 V ($\text{Co}^{\text{III}}-\text{N}\equiv\text{C}-\text{Fe}^{\text{III/II}}$), which corresponds to a change in the Fe-*L* spectra in **Figure 3b**. However, even in the fully charged sample, the Fe-*L* spectrum is composed of a mixture of Fe^{II} and Fe^{III} spectra, which is expected since the oxidation is limited by the number of sodium ions that can be extracted and not by the oxidation state of Fe. In fact, the composition of CoHCFE is $\text{Na}_{1.54}\text{Co}[\text{Fe}(\text{CN})_6]_{0.86}\cdot\text{□}_{0.14}\cdot 2.16\text{H}_2\text{O}$ in the fully reduced state. Fully charging the electrode would completely oxidize Co^{II} to Co^{III} and only oxidize 68% of Fe^{II} since the Fe redox potential is higher than that of Co in CoHCFE.

The Fe redox potential of CoHCFE is unexpectedly 200-300 mV higher than that of other hexacyanoferrate compounds³⁷. The increased potential is due to a modification of the band structure from increased p-d hybridization between N and Co^{III} ³⁸, and that is due to a lattice contraction triggered by the formation of LS Co^{III} ³⁸.

The Fe-*L* and Co-*L* spectra of CoHCFE are reported in **Figure 3b** and **3c**, respectively. The results are rather surprising. In fact, at lower potentials, the N-coordinated Co is electrochemically active ($\text{Co}^{\text{III/II}}-\text{N}\equiv\text{C}-\text{Fe}^{\text{II}}$), which corresponds to major changes in the Co-*L* spectra in **Figure 3c**. In particular, the growth of a sharp peak around 781 eV corresponds to the formation of an anomalous LS Co^{III} state. This LS state occurs despite the low crystal field splitting experienced by Co because of the stability of the LS d^6 electron configuration, and it is further enhanced by the significant lattice contraction of the framework³⁸, as described below.

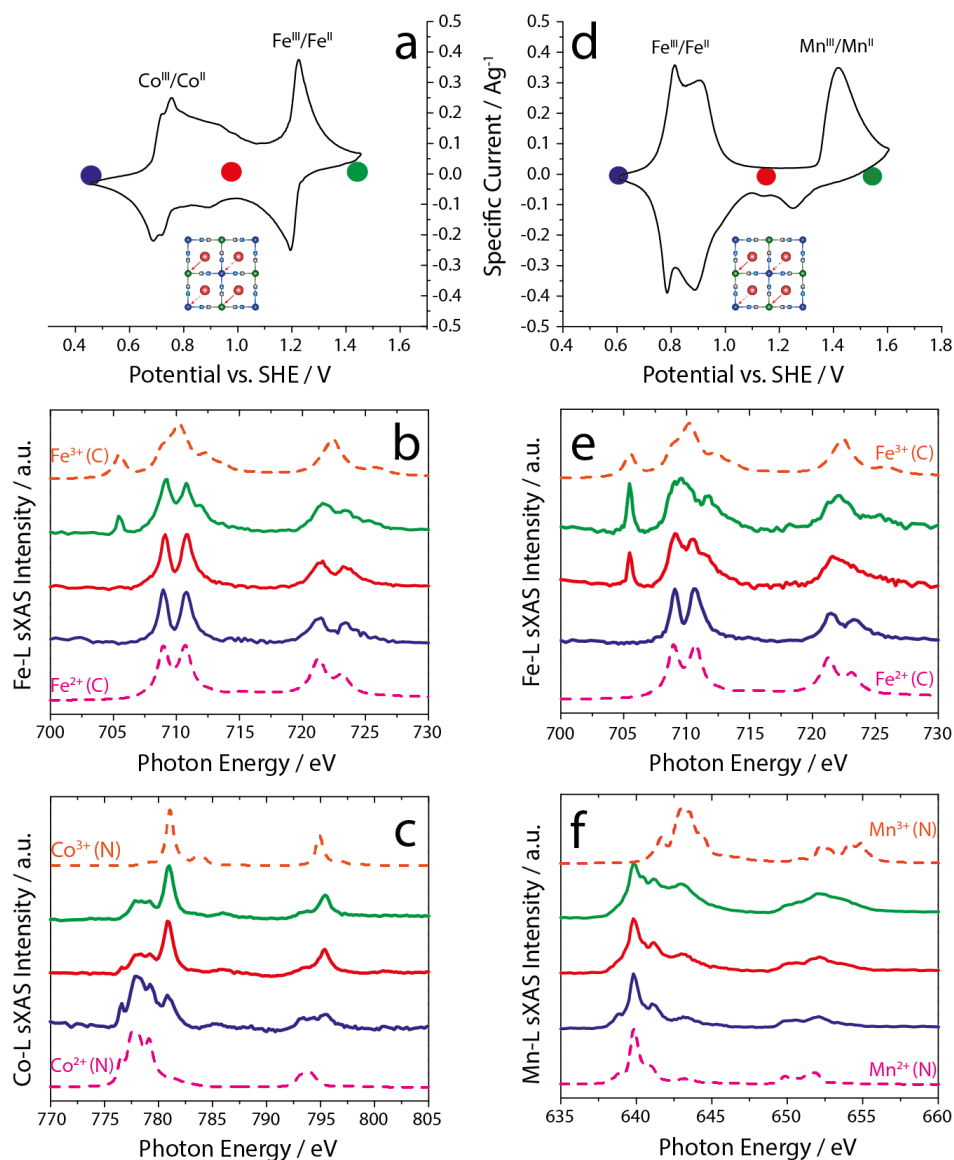


Figure 3. CoHCF and MnHCF electrochemistry with sXAS. The cyclic voltammograms (CV) of (a) CoHCF and (d) MnHCF in a pH=2, saturated NaClO₄ aqueous electrolyte show three electrochemical processes at 0.7, 0.75, and 1.2 V and at 0.8, 0.9, and 1.4 V, respectively. CoHCF and MnHCF electrodes for the sXAS studies were galvanostatically charged to three different potentials/charge states represented by the blue (0.6 V for MnHCF and 0.45 V for CoHCF), red (1.1 V and 0.95 V, respectively), and green (1.5 V and 1.45 V, respectively) dots. The two lower-potential processes are ascribable to the Na-ion insertion in rhombohedral and cubic phases, respectively. The experimental sXAS spectra (thicker lines) at Fe, Co, and Mn *L*-edges were collected on a series of (b-c) CoHCF and (e-f) MnHCF electrode samples cycled to different states of charge. The simulated spectra of C-coordinated Fe and N-coordinated Co or Mn are plotted in thinner, dashed lines.

Moreover, the Co redox potential is suppressed because of the stability of the d^6 LS Co^{III}. The CV reported in **Figure 3a** shows features consistent with this explanation. The broadened Co^{III/II} peak may be associated with a gradual rearrangement of the electronic structure as the LS Co^{III} is reduced to HS Co^{II} ³⁸. The two lower-potential processes are attributed to the Na-ion extraction from rhombohedral (0.7 V) and cubic (0.75 V) phases triggered by the previously described Na-ion displacement along the $\langle 111 \rangle$ directions. As the material is

oxidized, Na ions are extracted from the A sites, and the structure changes into the ordered cubic phase. These structural changes are shown in the crystallography section below.

The Fe-L and Mn-L spectra of MnHCFe are reported alongside the calculated Fe^{II}, Fe^{III} and Mn^{II}, Mn^{III} spectra in **Figure 3e** and **Figure 3f**, respectively. At 0.6 V (blue curves), Fe and Mn are both in their +2 oxidation state, as expected. When the potential is raised to 1.1 V (red curves), Fe^{II} is partially oxidized to Fe^{III}, and there are also some minor changes in the Mn spectra. At the highly oxidative potential of 1.5 V (green curves), we observe that Fe is oxidized further (especially evident in the growth of the peak at 706 eV), while Mn undergoes additional change. Although the Fe spectrum changes more at lower potential and the Mn spectrum at higher potential, Fe and Mn are both affected at the same time when the system loses electrons, unlike in the case of CoHCFe. This suggests that electrons may spontaneously hop from Fe to Mn, unlike in the case of CoHCFe; this hypothesis is supported by the *in situ* XRD data presented later. Mn^{III} sXAS spectra often have less precise correspondence with multiplet calculations, and the near-degeneracy of Mn and Fe electron acceptor states adds a further complication to the physical picture³⁰, so it is difficult to assess the degree of Mn oxidation when the electrode is fully charged.

The electrochemical processes at 0.8 and 0.9 V are mainly ascribable to the electrochemical activity of the C-coordinated Fe (Mn^{II}—N≡C—Fe^{III/II}), and they correspond to the extraction of Na ions from the rhombohedral and cubic phases, respectively. The N-coordinated Mn is instead primarily responsible for the poorly reversible electrochemical process at 1.4 V (Mn^{II/III}—N≡C—Fe^{III}). The source of this irreversibility can be ascribed to the combined effects of internal charge-transfer processes, hybridization between the Mn and N orbitals, and the oxidation of the aqueous electrolyte at this elevated potential. These are discussed further in the crystallography section below.

The calculated occupancies of the d-electron orbitals are listed in **Table 2**. Details about the calculations can be found in the methods section of the **Supporting Information**. Electrons transfer from the t_{2g} to the e_g orbitals in Co upon reduction, which corresponds to the spin-state transition from LS Co^{III} to HS Co^{II} previously described. In addition, the substantial increase in electron occupancy of the e_g orbitals strongly affects the Co-N bond length due to the orientation of the e_g orbitals along the axis of the bond. These short-range interactions between the Co and N orbitals drive a significant lattice expansion that is demonstrated with *in situ* XRD below. When HS Mn^{III} is reduced to HS Mn^{II}, electrons are only added to the e_g orbitals. This also induces a rapid lattice expansion because of the orientation of the e_g orbitals.

The weak crystal field experienced by the N-coordinated TM favors a HS state, which guarantees that electrons are mainly transferred to and from the e_g orbitals. The strong interaction between these orbitals and the N *sp* orbitals explains why redox reactions on the N-coordinated metal ion tend to have a greater impact on the crystal structure. Conversely, the strong crystal field experienced by the C-coordinated metal ion favors a LS state, so electrons are mainly transferred to and from the t_{2g} orbitals. As a result, the more indirect interactions between the t_{2g} orbitals and the C *sp* orbitals affect the structure to a lesser degree.

Table 2. Calculated *d*-electron occupancy for each of the configurations in CoHCF_e and MnHCF_e.

<i>d</i> electron occupancy			
	t_{2g}	e_g	total
Co³⁺(N)	5.931	0.483	6.414
Co²⁺(N)	4.893	2.244	7.138
Diff.	-1.038	1.761	0.724
Mn³⁺(N)	3.001	1.494	4.495
Mn²⁺(N)	3.000	2.081	5.081
Diff.	-0.001	0.587	0.586
Fe³⁺(C)	4.767	0.305	5.072
Fe²⁺(C)	5.548	0.150	5.698
Diff.	0.781	-0.155	0.626

When the C-coordinated Fe goes from Fe^{III} to Fe^{II}, there's a transfer of charge density from the e_g to t_{2g} orbitals. Taken on its own, such a transfer of charge density would be expected to make the lattice smaller, which compensates for the additional electron density added to the bond. This may also explain why the lattice stays roughly the same size when Fe cycles but expands when Co or Mn go from 3+ to 2+ (see below). More generally, less than one electron is added to the *d* orbitals when any of the TM is reduced, which reflects the itinerant nature of the *d*-electrons and transfer of charge between the TM and the cyano ligand³⁹.

Battery performance of CoHCF_e/MnHCF_e mixtures. CoHCF_e possesses more rapid and reversible electrochemical reactions than those of MnHCF_e (examined in detail in later sections). However, MnHCF_e has a higher reaction potential, which can contribute to higher energy and power densities. Single-phase mixtures of MnHCF_e and CoHCF_e may be able to combine desirable electrochemical features of both compounds. The CVs of the manganese-cobalt hexacyanoferrates (Mn-CoHCF_e) solid solutions are reported in **Figure 4a**. The insertion potentials increase linearly with the Mn content. A similar behavior has been previously observed for single-phase Cu-NiHCF_e mixtures⁸. Unfortunately, the irreversibility introduced by oxidation of the aqueous electrolyte and phase instability of Mn-containing mixtures decreases the energy and coulombic efficiencies of all these derivatives, thus limiting their practical application.

CoHCF_e shows a promising discharge capacity of 100 mAh g⁻¹ at C/2 and an average discharge potential of 1 V (**Figure 4b**). Electrochemical cycling of the N-coordinated Co significantly improves the specific capacity of PBAs in aqueous electrolyte beyond the 60 mAh g⁻¹ previously reported for CuHCF_e (black curves in **Figure 4b-c**) and at a similar discharge potential. On the other hand, the poor kinetics of the N-coordinated Co redox reaction (detailed in later sections) reduces the capacity retention at higher C rates (**Figure 4c, d**).

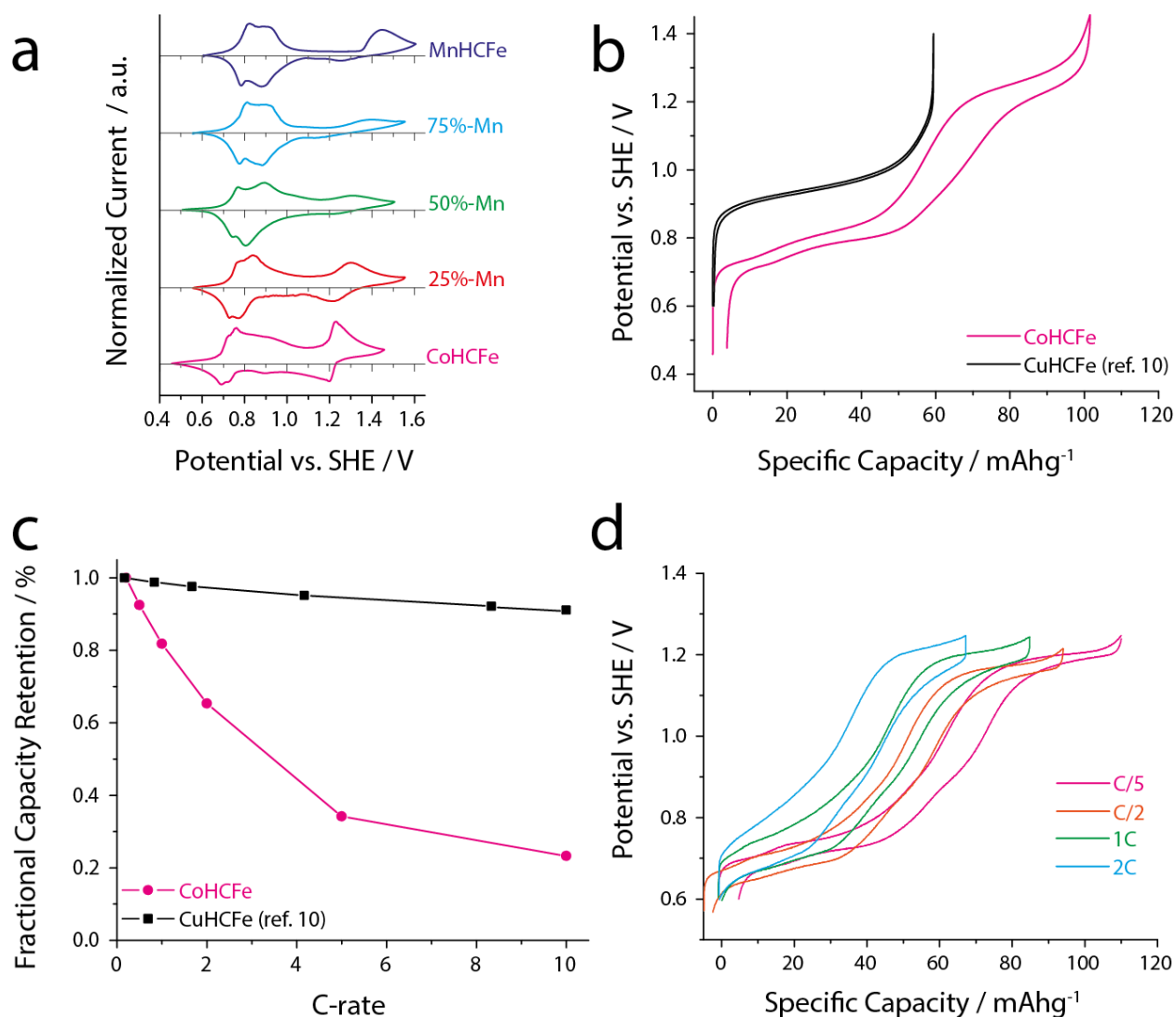


Figure 4. Battery performance of Mn-CoHCF solid solutions. The CVs at 1 mVs⁻¹ of the manganese-cobalt hexacyanoferrates solid solutions (**a**) show how the insertion potentials increase linearly with the Mn content. CoHCF shows a promising discharge capacity of 100 mAh g⁻¹ at C/2 and an average discharge potential of 1 V (**b**, pink curve). Electrochemical cycling of the N-coordinated Co significantly improves the specific capacity of PBAs in aqueous electrolyte beyond the 60 mAh g⁻¹ previously reported for CuHCF (**b**, black curve) at a similar discharge potential. On the other hand, the diffusion-limited N-coordinated Co redox reaction reduces the capacity retention at higher C rates (**c**, **d**). Panel (**c**) shows the fractional capacity retention of CoHCF (pink curve) and CuHCF (black curve) at different C-rates (0.2, 0.5, 1, 2, 5, 10 C). Panel (**d**) shows the galvanostatic charge-discharge profiles of CoHCF at 0.2, 0.5, 1, and 2 C.

In situ synchrotron X-ray diffraction. In situ synchrotron X-ray diffraction studies were performed on CoHCF and MnHCF in order to connect electrochemical properties to changes in the crystal structure. The results are reported in **Figure 5** (results on the 50% Mn-CoHCF solid solution are reported in **Figure S6**). Panels **a** and **d** show the galvanostatic charge-discharge curves at a 1C rate (black curves) and the lattice parameters (red curves) of the two materials as a function of the state of charge (the procedure for determining the rhombohedral/cubic lattice parameters is outlined in the methods section of the **Supporting Information**). Panels **b** and **e** show the waterfall plots of the in situ synchrotron XRD as a function of different charge states. The y-axis (specific capacity) is shared with panels **a** and

d. Higher peak intensities correspond to a brighter yellow color. This plot highlights trends in changing lattice parameter and phase transitions upon cycling. Finally, panels **c** and **f** display individual diffraction patterns (corrected 1D-slices from area detector images) at selected states of charge to accentuate changes in peak intensities and shapes.

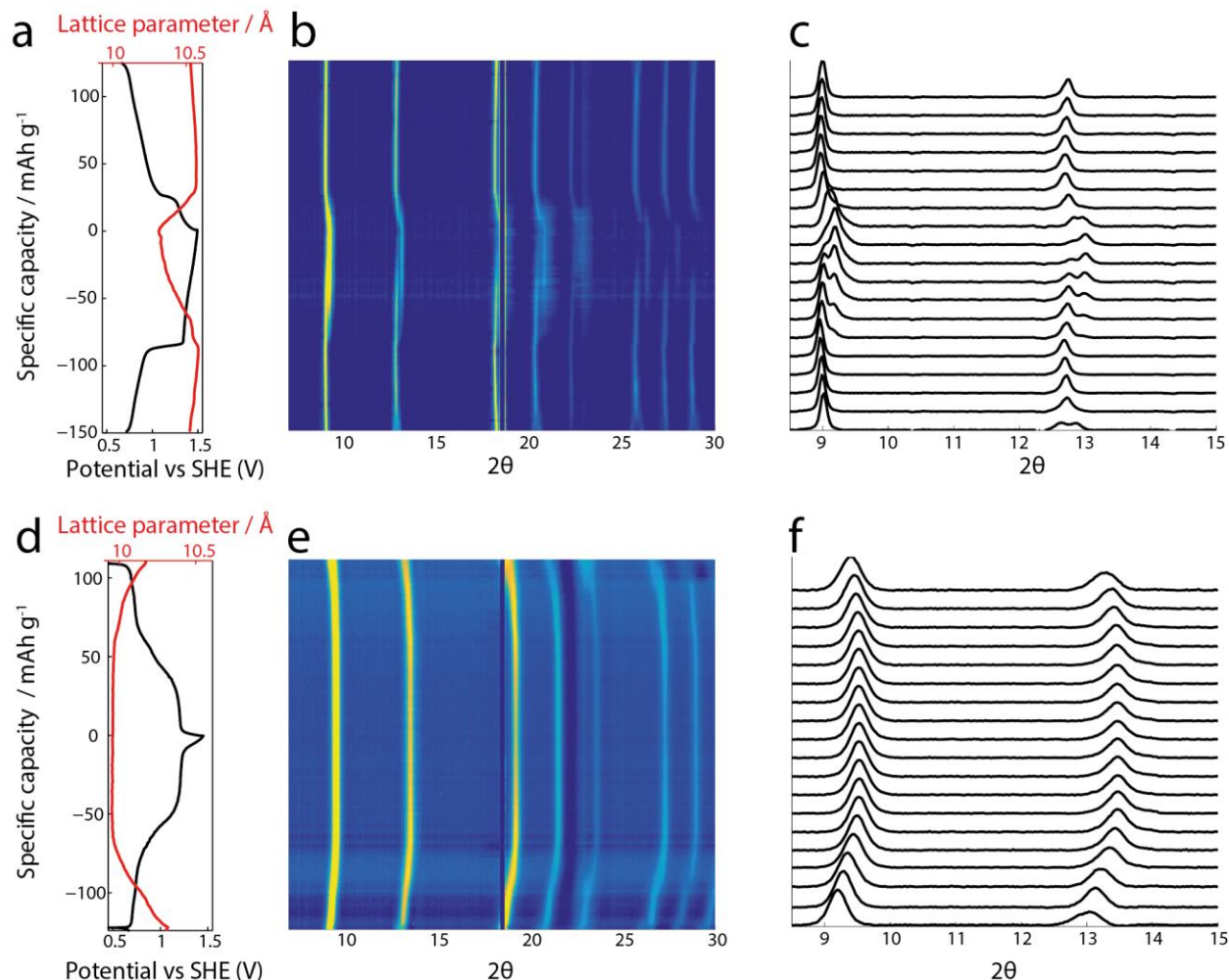


Figure 5. In situ synchrotron X-ray diffraction. Panels (a) and (d) show the galvanostatic charge-discharge curves at a 1C rate (black curve) and the cubic and rhombohedral lattice parameters (depending on the phase) (red curve) of MnHCF and CoHCF, respectively, as a function of the state of charge. Panels (b) and (e) show the waterfall plots of the in situ synchrotron XRD measured at different charge states for the same two materials. The stripe around 18° is a result of the gap between adjacent X-ray detectors. The y-axis (specific capacity) is shared with panels (a) and (d). Higher peak intensities correspond to a brighter yellow color. This plot highlights trends in changing lattice parameter and phase transitions upon cycling. Panels (c) and (f) display individual diffractograms at selected states of charge that accentuate changes in peak intensities and widths.

The results for MnHCF are reported in **Figure 5a-c**. Two redox plateaus are clearly visible in **Figure 5a** at 0.6 V and 1.4 V, roughly corresponding to $\text{Mn}^{\text{II}}-\text{N}\equiv\text{C}-\text{Fe}^{\text{III/II}}$ and $\text{Mn}^{\text{III/II}}-\text{N}\equiv\text{C}-\text{Fe}^{\text{III}}$, respectively, as described in the previous section. In **Figure 5b**, at lower charge states, the peak around 9° 2θ , attributed to the $\{202\}$ diffraction peak in the initial hexagonal lattice (rhombohedral distortion in primitive unit cell), shifts slightly towards lower angles upon initial charging. This signifies a slight increase in the rhombohedral lattice parameter (**Figure 5a**). This increase in lattice parameter has been previously observed when the C-

coordinated Fe atom in PBAs is electrochemically active, and it can be attributed to the smaller size of $[\text{Fe}(\text{CN})_6]^{4-}$ compared to $[\text{Fe}(\text{CN})_6]^{3-}$. This is because the $\text{Fe}^{\text{II}}-\text{C}$ bond length is shorter than that of $\text{Fe}^{\text{III}}-\text{C}^{40}$.

Moreover, it can be clearly seen both in **Figure 5b** and even more clearly in **Figure 5c** that at around $13^\circ 2\theta$ the original $\{220\}$ and $\{20\cdot4\}$ hexagonal peaks converge into a single peak upon initial charging. This corresponds to the rhombohedral-cubic transition observed in the CV curve in **Figure 3d** and as previously described.

As soon as the $\text{Mn}^{\text{II}}-\text{N}\equiv\text{C}-\text{Fe}^{\text{III/II}}$ transition is complete, the potential in the galvanostatic curve increases, and the second plateau ($\text{Mn}^{\text{III/II}}-\text{N}\equiv\text{C}-\text{Fe}^{\text{III}}$) at 1.4 V can be observed. At the same time, a phase separation occurs, as indicated by the appearance of secondary peaks at higher angles than those of the original. This is the result of the formation of Mn^{III} . Electrons are removed only from the e_g orbitals, which experience strong short-range interactions with the adjacent N atoms due to the orientation of the orbitals along the bond. This causes a significant contraction of the Mn-N bond (the ionic radius changes from 0.83 to 0.65 Å for Mn^{II} and Mn^{III} , respectively) and leads to localized strain⁴¹. Moreover, HS Mn^{III} experiences Jahn-Teller distortion, which further contributes to the structural strain. The rapid decrease in the lattice parameter triggers the spontaneous formation of a secondary cubic phase⁴¹.

During the discharge (reduction) step, the process is reversed: the N-coordinated Mn is reduced from Mn^{III} to Mn^{II} with a corresponding increase in lattice parameter and a return to the intermediate cubic phase. In this case, the phase separation happens very quickly and is not as clearly resolved in the XRD data. The reason is that during the charging step, part of the oxidation current does not flow to the MnHCFE active material but instead goes to the decomposition of the aqueous electrolyte. This reduces the effective C-rate at the upper redox plateau of MnHCFE and allows us to clearly observe the phase separation.

Upon further discharge, the C-coordinated Fe is reduced from Fe^{III} to Fe^{II} at 0.7 V, and there is a corresponding slight decrease in the lattice parameter. It appears that after one full cycle, MnHCFE does not completely convert to the original rhombohedral phase but retains the face-centered cubic crystal structure. We believe this may be due to both slow kinetics for the formation of the rhombohedral phase and incomplete reduction of MnHCFE back to the original redox state.

As previously noted, the discharge capacity on the upper Mn redox plateau is much smaller than the corresponding charge capacity, which may be partially attributable to electrolyte decomposition. On the other hand, the discharge capacity on the lower Fe redox plateau (about 100 mAh g^{-1}) is much higher than the corresponding charge capacity (about 65 mAh g^{-1}). This may also help to explain the small discharge capacity of the higher-potential Mn plateau. Electrons spontaneously transfer from Fe to Mn would cause the unbalanced capacities on both Fe and Mn. The extra electrons on Mn would increase its capacity during charge and decrease its capacity during discharge, and the missing electrons on Fe would have the opposite effect on its capacities.

Analogous instances of hysteresis and irreversibility in temperature-induced phase transitions have been observed in MnHCFe and can be attributed to spontaneous and asymmetric charge-transfer and hybridization across the C≡N bond between Mn and Fe⁴². This phenomenon makes it challenging to attribute features in the electrochemical data exclusively to separate redox processes in MnHCFe.

Figure 5a can also provide additional insight into the electrochemical performance of MnHCFe. It can be clearly observed that the overall charge-discharge cycle has a low coulombic efficiency (83%). The main reason is that, during oxidation, the Mn^{II/III}—N≡C—Fe^{III} step occurs at a potential above the electrochemical stability window of the aqueous electrolyte. The electrochemical process is therefore in competition with the oxidation of water to oxygen, an irreversible process that consequently limits the overall coulombic efficiency. Such a low coulombic efficiency is obviously not compatible with practical applications. We can therefore conclude that pure MnHCFe is not a suitable positive electrode candidate for aqueous NIBs.

Figure 5d-f show the results of the in situ XRD study of CoHCFe. The galvanostatic charge/discharge curve (**Figure 5d**) shows two electrochemical processes. The sXAS results confirm that the one at 0.7 V corresponds to Co^{III/II}—N≡C—Fe^{II}, and the one at 1.2 V corresponds to Co^{III}—N≡C—Fe^{III/II}. As the N-coordinated Co^{II} is oxidized, the lattice parameter decreases. This is due to the larger ionic radius of the HS Co²⁺ (0.745 Å) compared to the LS Co³⁺ (0.545 Å), as previously highlighted by Igarashi et al⁴³. In addition, the (422) cubic peak around 2θ = 23° splits into two peaks. This may correspond to a slight distortion of the cubic structure that accommodates the contraction of the Co-N bond as it changes spin states.

In the high-voltage plateau, the C-coordinated Fe is electrochemically active, but no lattice parameter variation is observed. We believe this is due to hybridization processes across the cyano groups associated with the peculiar spin states of CoHCFe previously described⁴⁴. It is noteworthy to mention that when C-coordinated Fe goes from Fe^{III} to Fe^{II}, there's a transfer of charge density from the *e_g* to *t_{2g}* orbitals. Taken on its own, such a transfer of charge density would be expected to make the lattice smaller. This may partly explain why the lattice stays roughly the same size when Fe cycles but expands when Co or Mn go from 3+ to 2+.

Figure 5e-f clearly show how CoHCFe, unlike MnHCFe, does not experience an abrupt formation of a new phase but only a slight atomic rearrangement resulting in a rhombohedral-cubic ordering in the low-voltage plateau. This ordering can also be observed at low voltage in the CoHCFe CV. From an electrochemistry perspective, the charge/discharge profile reflects the high reversibility and coulombic and energy efficiencies of the material. This is directly attributable to the phase stability of CoHCFe across a wide voltage range.

The 50% Mn-CoHCFe reported in **Figure S6** exhibits features similar to those from both CoHCFe and MnHCFe.

Electrochemical investigation. The galvanostatic intermittent titration technique (GITT) is a powerful method that provides both thermodynamic and kinetic information about the electrochemical system under investigation. In this experiment, constant current pulses

followed by relaxation periods are applied to the electrode while measuring its potential variation as a function of time (**Figure S7a**). If the relaxation steps are long enough to allow the system to reach thermodynamic equilibrium, the potential versus composition phase diagram of the system under investigation can be determined (**Figure 6a-b**). Moreover, by measuring the thermodynamic potential changes (ΔE_T) between two equilibrium compositions and during the current pulse (ΔE_K), the chemical diffusion coefficient (or effective diffusion coefficient) D can be calculated according to the following equation⁴⁵:

$$D = \frac{4}{\pi\tau} \left(\frac{mV_M}{M_w S} \right)^2 \left(\frac{\Delta E_T}{\Delta E_K} \right)^2 \quad (1)$$

where τ is the pulse time, m , V_M , and M_w are the sample mass, the molar volume, and the molecular weight, respectively, and S is the contact area between the active material and the electrolyte. The relationship is valid when small pulses are applied (i.e. $\tau < L^2/D$ where L is the diffusion length).

The MnHCFE composition/potential phase diagram (**Figure 6b**) clearly shows two different regions that can be attributed to the redox processes of the two transition metal cations, in full agreement with the sXAS and CV reported in **Figure 3d-f**. The monotonic potential increase up to 75 mAh g⁻¹ (0.7 Na ions per Mn) indicates that the Mn^{III}—N≡C—Fe^{III/II} electrochemical process takes place in a single-phase system. The diffusion coefficient calculated according to **Equation 1** is on the order of 10⁻⁷ cm² s⁻¹ and depends on the phase composition (**Figure S7b**). Of particular interest is the D value corresponding to the composition Na_{1.05}Mn[Fe(CN)₆]_{0.79}, which can be compared with the diffusion coefficient obtained by EIS discussed later in the text. The constant potential profile during the Mn^{III/II}—N≡C—Fe^{III} redox process is the result of a biphasic system, which is consistent with the in situ XRD data reported. **Equation 1** cannot be applied in this case because $\Delta E_T=0$.

The CoHCFE composition/potential phase diagram (**Figure 6a**) shows that both redox processes occur within a single-phase domain, also in agreement with the structural data previously reported. The chemical diffusion coefficient is in the range 10⁻⁸-10⁻⁹ cm² s⁻¹ (see **Figure S7b**), which is substantially lower than that in MnHCFE.

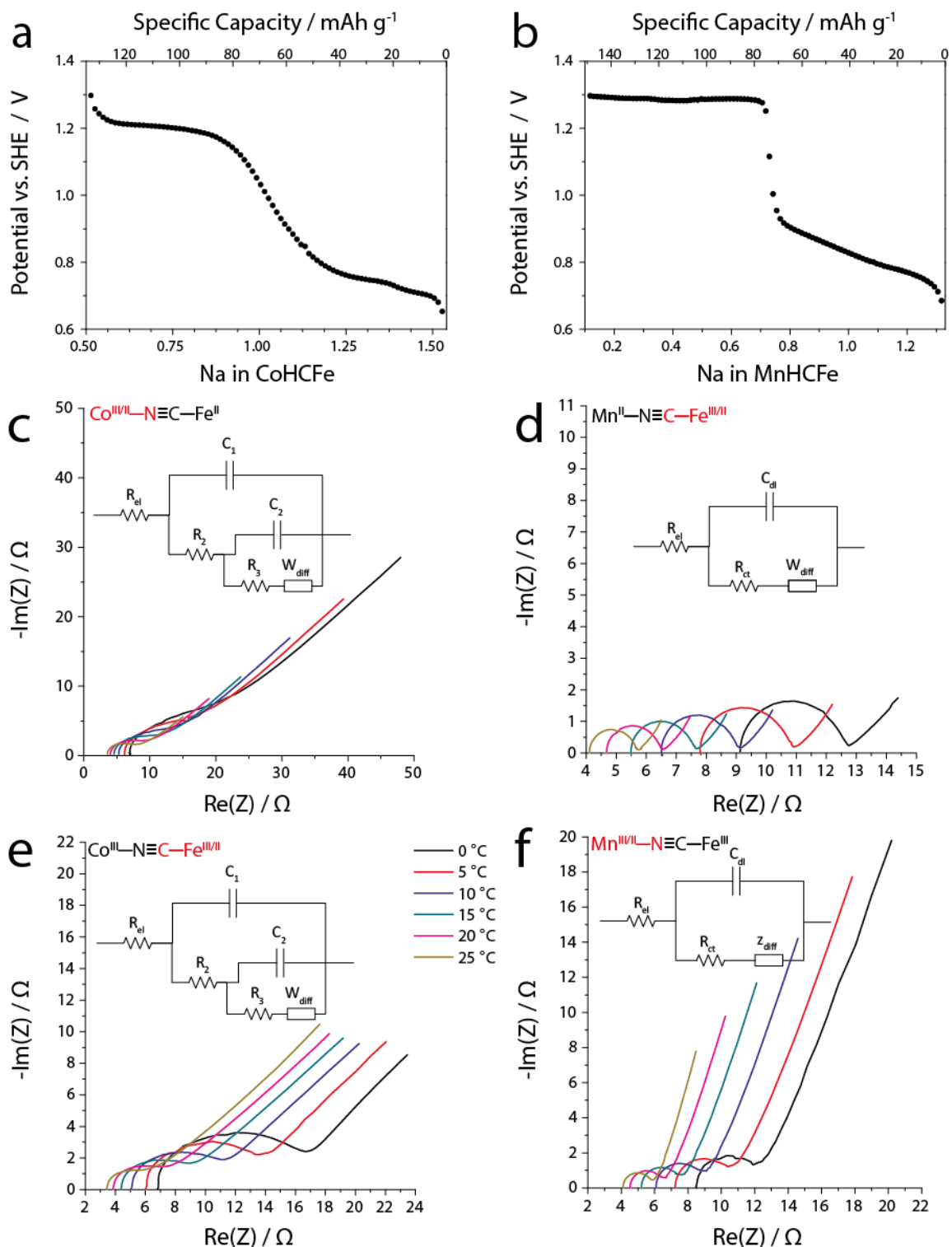


Figure 6. Electrochemical Characterization. Potential versus composition phase diagrams of CoHCF (a) and MnHCF (b) were determined by the galvanostatic intermittent titration technique (GITT). Potentiostatic electrochemical impedance spectroscopy measurements were taken at different temperatures in the 0-25 °C range of the (c) $\text{Co}^{\text{III/II}}-\text{N}\equiv\text{C}-\text{Fe}^{\text{II}}$, (e) $\text{Co}^{\text{III}}-\text{N}\equiv\text{C}-\text{Fe}^{\text{III/II}}$, (d) $\text{Mn}^{\text{II}}-\text{N}\equiv\text{C}-\text{Fe}^{\text{III/II}}$, and (f) $\text{Mn}^{\text{III/II}}-\text{N}\equiv\text{C}-\text{Fe}^{\text{III}}$ electrochemical processes. The Randles circuits used to model each electrochemical process are also reported.

Potentiostatic electrochemical impedance spectroscopy (EIS) measurements at different temperatures in the 0-25 °C range were used to model each electrochemical process and extract the corresponding activation energies. **Figure 6d** shows the EIS spectra for $\text{Mn}^{\text{II}}-\text{N}\equiv\text{C}-\text{Fe}^{\text{III/II}}$ and the Randles equivalent circuit used to fit the experimental data. The parameters we are interested in are the charge-transfer resistance (R_{ct}) and the Warburg diffusion resistance (W_{diff}), which are characteristic of the electrochemical process investigated. Resistance of the electrolyte (R_{el}) and double-layer capacitance (C_{dl}) are similar for all the processes since the electrolyte and surface area are the same for both samples. By plotting $\ln(R_{\text{ct}}^{-1})$ and $\ln(W_{\text{diff}}^{-1})$ as a function of the inverse of the temperature (Arrhenius plot, **Figure S8-S9**), we can calculate the corresponding activation energy values: 0.26 eV (R_{ct}) and 0.17 eV (W_{diff}). From the Warburg impedance, it is also possible to measure the chemical diffusion coefficient D by using the relationship developed by Ho et al.⁴⁶:

$$W = \left| \frac{V_M \frac{dE}{dx}}{\sqrt{2} z F \sqrt{D} A} \right|$$

where V_m is the molar volume and dE/dx is the slope of the potential/composition profile in equilibrium conditions. This latter value can be easily obtained from the corresponding GITT profiles. By using the Ho equation, the D value related to the $\text{Mn}^{\text{II}}-\text{N}\equiv\text{C}-\text{Fe}^{\text{III/II}}$ process at 20°C is $4.5 \pm 0.5 \times 10^{-7} \text{ cm}^2 \text{ s}^{-1}$. The value is in good agreement with the value calculated by GITT at the same composition, i.e. $1.3 \pm 1.0 \times 10^{-7} \text{ cm}^2 \text{ s}^{-1}$.

Figure 6f reports the same EIS investigation for the $\text{Mn}^{\text{III/II}}-\text{N}\equiv\text{C}-\text{Fe}^{\text{III}}$ process. In this case, an anomalous diffusion model (Z_{diff}) better fits the experimental data. In fact, the bi-phasic nature of the system complicates the diffusion representation through a simple finite or semi-infinite model. The values of the activation energies for the two processes are 0.26 eV and 0.39 eV for the charge-transfer and diffusion processes, respectively. The higher activation energy associated with the diffusion process (relative to that of CoHCFe) may derive from the phase separation that occurs as ions are removed.

A more complex model needs to be applied in order to fit the EIS experimental data of the two electrochemical processes in CoHCFe. In the proposed Randles circuit for both $\text{Co}^{\text{III/II}}-\text{N}\equiv\text{C}-\text{Fe}^{\text{II}}$ (**Figure 6c**) and $\text{Co}^{\text{III}}-\text{N}\equiv\text{C}-\text{Fe}^{\text{III/II}}$ (**Figure 6e**), two different charge-transfer resistances (R_2 and R_3) can be observed. As a consequence of the extensive orbital hybridization within CoHCFe, the distinction between the two processes is not as neat as in the case of MnHCFe, and the contribution of both ions is observed in the entire potential range. This is not observed in the sXAS results and simulations because those are measured at equilibrium, while the EIS results are measured while the sample is perturbed. Thus, even though we see both Co and Fe reactions in each process in EIS, internal charge-transfer causes the electrons to be distributed on either Co or Fe at equilibrium.

For both processes, we observe two resistances that correspond to Co and Fe charge transfer. In fact, for both processes, the activation energy of one of the two resistances is very similar to the activation energy of the C-coordinated Fe in MnHCFe (0.23 and 0.26 eV for the $\text{Co}^{\text{III/II}}-\text{N}\equiv$ and the $\equiv\text{C}-\text{Fe}^{\text{III/II}}$ processes in CoHCFe, respectively). The other resistance has instead a higher value and is very similar in the two processes (0.34 and 0.36 eV for the $\text{Co}^{\text{III/II}}-\text{N}\equiv$

and the $\equiv\text{C}-\text{Fe}^{\text{III/II}}$ processes, respectively) and we believe it is ascribable to the electrochemical activity of the N-coordinated Co.

In the case of $\text{Co}^{\text{III/II}}-\text{N}\equiv\text{C}-\text{Fe}^{\text{II}}$ (**Figure 6c**), the activation energy of the total surface reaction (i.e. R_2+R_3) is 0.28 eV, which is lower than the activation energy for the diffusion process (0.48 eV). The activation energy of this total surface reaction is similar to those of Mn and Fe in MnHCFE (0.26 eV). The activation energy of the diffusion process in $\text{Co}^{\text{III/II}}-\text{N}\equiv\text{C}-\text{Fe}^{\text{II}}$ is higher than those in MnHCFE.

Diffusion coefficients at 20°C for CoHCFE can be calculated using EIS data from the equation by Ho et al. previously reported. The diffusion coefficient for $\text{Co}^{\text{III/II}}-\text{N}\equiv\text{C}-\text{Fe}^{\text{II}}$ is $1.6\pm0.5\times10^{-9}\text{ cm}^2\text{ s}^{-1}$, while the value for $\text{Co}^{\text{III}}-\text{N}\equiv\text{C}-\text{Fe}^{\text{III/II}}$ is $1.4\pm0.5\times10^{-9}\text{ cm}^2\text{ s}^{-1}$. The values are in full agreement with the results of the GITT analysis (**Table 3**).

Table 3. Diffusion coefficients summary at 20°C.

Method	Co in CoHCFE	Fe in CoHCFE	Mn in MnHCFE	Fe in MnHCFE
EIS @ 20°C	$1.6\pm0.5\text{E-}09$	$1.4\pm0.5\text{E-}09$	NA (biphasic)	$4.5\pm0.5\text{E-}07$
GITT	$1.1\pm0.2\text{E-}09$	$1.9\pm0.5\text{E-}09$	NA (biphasic)	$1.3\pm1.0\text{E-}07$

The kinetic regime in each of the electrochemical processes observed in both MnHCFE and CoHCFE can also be understood by analyzing the relationship between the CV scan rate and the corresponding peak current (**Figure S10**).

Discussion

Increasing the specific capacity of PBA materials for grid-scale energy storage applications can be achieved by exploiting the electrochemical activity of the N-coordinated transition metal ion. The only PBAs that demonstrate electrochemical activity of both C- and N-coordinated ions within the stability window of an aqueous electrolyte are the hexacyanoferrates of manganese and cobalt³⁷. The electrochemical processes associated with the C-coordinated ions in PBAs do not have a major impact on the crystal structure. As a result, these reactions exhibit high reversibility and rapid electrochemistry. This desirable behavior enables the faster discharge rates, high energy efficiencies, and long cycle lives previously reported for CuHCFE⁹, NiHCFE¹⁰, and MnHCMn^{18,19}.

On the other hand, the electrochemistry of the N-coordinated ions displays slower kinetics and irreversibility. The poor electrochemical behavior is attributable to significant crystallographic modification of the open framework structure when Co or Mn is cycled, which hinders the solid-state diffusion of sodium ions in the structure. In the case of MnHCFE, Jahn-Teller distortion associated with the formation of the Mn^{III} species also promotes a phase separation. As for CoHCFE, the energetic stability of the LS d^6 electron configuration promotes a HS-LS $\text{Co}^{\text{II}}/\text{Co}^{\text{III}}$ transition, and the LS state is further stabilized by the significant lattice contraction of the framework³⁸.

The electrochemical behavior clearly depends on the specific redox species in the material. However, more generally, the low crystal field experienced by the N-coordinated ion promotes HS states and also increases the probability of HS-LS transitions. In addition, the HS state causes electrons to be transferred to and from the e_g orbitals instead of the t_{2g} orbitals. The

strong interaction between the e_g orbitals and the sp N orbitals induces more significant distortions in the crystal structure compared to those caused by redox of the LS C-coordinated ion.

Practically speaking, MnHCFe offers two clear advantages: a higher insertion potential, which produces higher power and energy output; and a significantly lower material cost (\$2.20 versus \$30.60 per kg for Mn and Co, respectively⁴⁷). On the other hand, the upper plateau ($\text{Mn}^{\text{III/II}}-\text{N}\equiv\text{C}-\text{Fe}^{\text{III}}$) can only be accessed at a potential outside the stability limit of the optimized aqueous electrolyte (1.4 V). Moreover, the reaction is intrinsically irreversible because of a phase separation triggered by the Jahn-Teller distortion of Mn^{III} . As a result, all mixtures of MnHCFe and CoHCFe display poorer energy and coulombic efficiencies relative to those of CoHCFe.

CoHCFe possesses much better electrochemical reversibility in both of its redox reactions. The unusual energetic stability of LS Co^{III} lowers the redox voltage of the $\text{Co}^{\text{III/II}}$ reaction so that it is accessible within the electrolyte stability limit. The material also retains its basic crystal structure (with the exception of a minor rhombohedral-cubic ordering) throughout the entire range of cycling. CoHCFe offers a compelling balance of features suitable for grid-scale storage applications: rapid kinetics, high specific capacity in aqueous electrolyte relative to other PBAs, high energy and coulombic efficiencies, and stable cycling.

We have established direct relationships between the crystallography, electronic states, electrochemical reversibility, and kinetics of manganese- and cobalt-based hexacyanoferrates. The integration of in-depth electrochemical experiments, soft X-ray absorption spectroscopy, and in situ X-ray diffraction has provided powerful and novel insights into how these materials function. This experimental approach has not only expanded our understanding of Prussian Blue analogues but may also help to drive the development of such materials for grid-scale energy storage applications.

Acknowledgments

The authors would like to acknowledge support from the Global Climate and Energy Project (GCEP) at Stanford as well as the U.S. Department of Energy (DOE), Office of Electricity Delivery & Energy Reliability for this research through collaboration with the Pacific Northwest National Laboratory. Pacific Northwest National Laboratory is a multiprogram national laboratory operated for DOE by Battelle under Contract DEA C05-76RL01830. Use of the Stanford Synchrotron Radiation Lightsource, SLAC National Accelerator Laboratory, is supported by the U.S. Department of Energy, Office of Science, Office of Basic Energy Sciences under Contract No. DE-AC02-76SF00515. Use of the Advanced Light Source, Lawrence Berkeley National Laboratory, is supported by the Director, Office of Science, Office of Basic Energy Sciences, of the U.S. Department of Energy under Contract No. DE-AC02-05CH11231. M.P. acknowledges the support of the Oronzio and Niccolò De Nora Foundation. R.Y.W acknowledges support from the National Science Foundation Graduate Research Fellowship and the National Defense Science & Engineering Graduate Fellowship. H.W.L. acknowledges support from the Basic Science Research Program through the National Research Foundation of Korea (NRF) funded by the Ministry of Education, Science and Technology under Contract No. 2012038593. Ruimin Qiao acknowledges support from the

Laboratory-Directed Research and Development (LDRD) program at the Lawrence Berkeley National Laboratory. M.G. is supported by China Scholarship Council Fellowship. R.R. acknowledges support from Fondazione Cariplo (contract 2011-0312).

Author contributions

M.P., R.Y.W., and R.R. designed electrochemical and physical measurements. M.P., R.Y.W., R.R., and H.W.L. performed and analyzed electrochemical measurements and physical characterization. M.P., R.Y.W., B.S., and M.F.T designed and performed the in situ synchrotron X-ray diffraction measurements. M.P., R.Y.W., R.Q., L.A.W., M.G., Y.W., and W.Y designed and performed the soft X-ray absorption measurements and analysis. L.A.W. performed the simulations of the sXAS spectra and d-electron occupancy numbers. M.P., R.Y.W., and Y.C. wrote this paper.

References

- (1) Yang, Z.; Zhang, J.; Kintner-Meyer, M. C. W.; Lu, X.; Choi, D.; Lemmon, J. P.; Liu, J. *Chem. Rev. (Washington, DC, United States)* **2011**, *111*, 3577.
- (2) Rastler, D. *EPRI Rep.* **2010**, 170.
- (3) Barnhart, C. J.; Dale, M.; Brandt, A. R.; Benson, S. M. *Energy Environ. Sci.* **2013**, *6*, 2804.
- (4) Barnhart, C.; Benson, S. *Energy Environ. Sci.* **2013**, *6*, 1083.
- (5) Rastler, D.; Kamath, H. *EPRI J.* **2010**, 20.
- (6) University of California, B. S. of L.; University of California, L. A.; University of California, S. D. **2011**.
- (7) Wessells, C. D.; Peddada, S. V.; McDowell, M. T.; Huggins, R. a.; Cui, Y. *J. Electrochem. Soc.* **2012**, *159*, A98.
- (8) Wessells, C. D.; McDowell, M. T.; Peddada, S. V.; Pasta, M.; Huggins, R. A.; Cui, Y. *ACS Nano* **2012**, *6*, 1688.
- (9) Wessells, C. D.; Huggins, R. A.; Cui, Y. *Nat. Commun.* **2011**, *2*, 550.
- (10) Wessells, C. D.; Peddada, S. V.; Huggins, R. A.; Cui, Y. *Nano Lett.* **2011**, *11*, 5421.
- (11) Yang, D.; Xu, J.; Liao, X.-Z.; Wang, H.; He, Y.-S.; Ma, Z.-F. *Chem. Commun. (Camb).* **2015**, *51*, 3.
- (12) Yu, S.; Li, Y.; Lu, Y.; Xu, B.; Wang, Q.; Yan, M.; Jiang, Y. *J. Power Sources* **2015**, *275*, 45.
- (13) Zhang, L.; Chen, L.; Zhou, X.; Liu, Z. *Adv. Energy Mater.* **2014**, *5*, 2.
- (14) Ludi, A.; Güdel, H. *Inorg. Chem.* **1973**, *14*, 1.
- (15) Herren, F.; Fischer, P.; Ludi, A.; Hälg, W.; Haelg, W. *Inorg. Chem.* **1980**, *19*, 956.
- (16) Buser, H. J.; Schwarzenbach, D.; Petter, W.; Ludi, A. *Inorg. Chem.* **1977**, *16*, 2704.
- (17) Wang, R. Y.; Wessells, C. D.; Huggins, R. a; Cui, Y. *Nano Lett.* **2013**, *13*, 5748.
- (18) Pasta, M.; Wessells, C. D.; Huggins, R. A.; Cui, Y. *Nat. Commun.* **2012**, *3*, 1149.
- (19) Pasta, M.; Wessells, C. D.; Liu, N.; Nelson, J.; McDowell, M. T.; Huggins, R. a; Toney, M. F.; Cui, Y.; Huggins, A. *Nat. Commun.* **2014**, *5*, 3007.
- (20) Guo, Y.-G.; You, Y.; Wu, X.-L.; Yin, Y.-X. *Energy Environ. Sci.* **2014**.
- (21) Wang, R. Y.; Shyam, B.; Stone, K. H.; Weker, J. N.; Pasta, M.; Lee, H.-W.; Toney, M. F.; Cui, Y. *Adv. Energy Mater.* **2015**, *5*, n/a.
- (22) Bhatt, P.; Thakur, N.; Mukadam, M. D.; Meena, S. S.; Yusuf, S. M. *J. Phys. Chem. C* **2013**, *117*, 2676.
- (23) Moritomo, Y.; Kurihara, Y.; Matsuda, T.; Kim, J. *J. Phys. Soc. Japan* **2011**, *80*, 1.
- (24) Moritomo, Y.; Matsuda, T.; Kurihara, Y.; Kim, J. *J. Phys. Soc. Japan* **2011**, *80*, 074608.
- (25) Wang, L.; Lu, Y. H.; Liu, J.; Xu, M. W.; Cheng, J. G.; Zhang, D. W.; Goodenough, J. B. *Angew. Chemie-International Ed.* **2013**, *52*, 1964.
- (26) Shannon, R. D. *Acta Crystallogr. Sect. A* **1976**, *32*, 751.
- (27) Yang, W.; Liu, X.; Qiao, R.; Olalde-Velasco, P.; Spear, J. D.; Roseguo, L.; Pepper, J. X.; Chuang, Y. De; Denlinger, J. D.; Hussain, Z. *J. Electron Spectros. Relat. Phenomena* **2013**, *190*, 64.
- (28) Qiao, R.; Lucas, I. T.; Karim, A.; Syzdek, J.; Liu, X.; Chen, W.; Persson, K.; Kostecki, R.; Yang, W. *Adv. Mater. Interfaces* **2014**, n/a.
- (29) Liu, X.; Liu, J.; Qiao, R.; Yu, Y.; Li, H.; Suo, L.; Hu, Y. S.; Chuang, Y. D.; Shu, G.; Chou, F.; Weng, T. C.; Nordlund, D.; Sokaras, D.; Wang, Y. J.; Lin, H.; Barbiellini, B.; Bansil, a; Song, X.; Liu, Z.; Yan, S.; Liu, G.; Qiao, S.; Richardson, T. J.; Prendergast,

- D.; Hussain, Z.; de Groot, F. M.; Yang, W. *J Am Chem Soc* **2012**, *134*, 13708.
- (30) Qiao, R.; Chin, T.; Harris, S. J.; Yan, S.; Yang, W. *Curr. Appl. Phys.* **2013**, *13*, 544.
- (31) Qiao, R.; Wang, Y.; Olalde-Velasco, P.; Li, H.; Hu, Y.-S.; Yang, W. *J. Power Sources* **2015**, *273*, 1120.
- (32) Wang, L.; Song, J.; Qiao, R.; Wray, L. A.; Hossain, M. A.; Chuang, D.; Yang, W.; Lu, Y.; Evans, D.; Lee, J.; Vail, S.; Zhao, X.; Nishijima, M.; Kakimoto, S.; Goodenough, J. B. **2015**.
- (33) Nanba, Y.; Asakura, D.; Okubo, M.; Zhou, H.; Amemiya, K.; Okada, K.; Glans, P.-A.; . Jenkins, C. A.; Arenholz, E.; Guo, J. *Phys. Chem. Chem. Phys.* **2014**, *16*, 7031.
- (34) Hocking, R. K.; Wasinger, E. C.; De Groot, F. M. F.; Hodgson, K. O.; Hedman, B.; Solomon, E. I. *J. Am. Chem. Soc.* **2006**, *128*, 10442.
- (35) Yang, Y.; Brownell, C.; Sadrieh, N.; May, J.; Del Grosso, A.; Place, D.; Leutzinger, E.; Duffy, E.; He, R.; Houn, F.; Lyon, R.; Faustino, P. *Clin. Toxicol.* **2007**, *45*, 776.
- (36) Wessells, C.; Ruffo, R.; Huggins, R. a.; Cui, Y. *Electrochem. Solid-State Lett.* **2010**, *13*, A59.
- (37) Scholz, F.; Dostal, A. *Angew. Chemie Int. Ed.* **1996**, *34*, 2685.
- (38) Kurihara, Y.; Moritomo, Y. *Jpn. J. Appl. Phys.* **2014**, *067101*, 0.
- (39) Asakura, D.; Nanba, Y.; Okubo, M.; Mizuno, Y.; Niwa, H.; Oshima, M.; Zhou, H.; Okada, K.; Harada, Y. *J. Phys. Chem. Lett.* **2014**, *5*, 4008.
- (40) Dostal, A.; Kauschka, G.; Reddy, S. J. J.; Scholz, F. *J. Electroanal. Chem.* **1996**, *406*, 155.
- (41) Kurihara, Y.; Matsuda, T.; Moritomo, Y. *Jpn. J. Appl. Phys.* **2013**, *52*, 017301.
- (42) Tokoro, H.; Ohkoshi, S.; Matsuda, T.; Hashimoto, K. *Inorg. Chem.* **2004**, *43*, 5231.
- (43) Igarashi, K.; Nakada, F.; Moritomo, Y. *Phys. Rev. B* **2008**, *78*, 235106.
- (44) Shimamoto, N.; Ohkoshi, S.; Sato, O.; Hashimoto, K. *Inorg. Chem.* **2002**, *41*, 678.
- (45) Weppner, W.; Huggins, R. *J. Electrochem. Soc.* **1977**, *124*.
- (46) Ho, C.; Raistrick, I.; Huggins, R. *J. Electrochem. ...* **1980**, *127*.
- (47) <http://mineralprices.com/>.